



Age effects and sex differences in human brain white matter of young to middle-aged adults: A DTI, NODDI, and q-space study



Chandana Kodiweera ^a, Andrew L. Alexander ^{b,c}, Jaroslaw Harezlak ^d, Thomas W. McAllister ^e, Yu-Chien Wu ^{f,*}

^a Department of Psychological and Brain Sciences and Dartmouth Brain Imaging Center, Dartmouth College, 6207, Moore Hall, Hanover, NH 03755, USA

^b Departments of Medical Physics and Psychiatry, School of Medicine and Public Health, University of Wisconsin, Madison, WI 53705, USA

^c Waisman Laboratory for Brain Imaging and Behavior, 1500 Highland Ave, Madison, WI 53705, USA

^d Department of Biostatistics, Richard M. Fairbanks School of Public Health and School of Medicine, Indiana University, 410 W 10th St., Suite 3000, Indianapolis, IN 46202, USA

^e Department of Psychiatry, Indiana University School of Medicine, Goodman Hall 355 W. 16th St., Suite 4800, Indianapolis, IN 46202, USA

^f Department of Radiology and Imaging Sciences, Indiana University School of Medicine, Goodman Hall, 355 West 16th Street, Suite 4100, Indianapolis, IN 46202, USA

ARTICLE INFO

Article history:

Received 25 June 2015

Accepted 18 December 2015

Available online 24 December 2015

Keywords:

White matter

Diffusion tensor

Fractional anisotropy

NODDI

Orientation dispersion index

Axonal density

Intra-cellular volume fraction

Aging

Sex

ABSTRACT

Microstructural changes in human brain white matter of young to middle-aged adults were studied using advanced diffusion Magnetic Resonance Imaging (dMRI). Multiple shell diffusion-weighted data were acquired using the Hybrid Diffusion Imaging (HYDI). The HYDI method is extremely versatile and data were analyzed using Diffusion Tensor Imaging (DTI), Neurite Orientation Dispersion and Density Imaging (NODDI), and q-space imaging approaches. Twenty-four females and 23 males between 18 and 55 years of age were included in this study. The impact of age and sex on diffusion metrics were tested using least squares linear regressions in 48 white matter regions of interest (ROIs) across the whole brain and adjusted for multiple comparisons across ROIs. In this study, white matter projections to either the hippocampus or the cerebral cortices were the brain regions most sensitive to aging. Specifically, in this young to middle-aged cohort, aging effects were associated with more dispersion of white matter fibers while the tissue restriction and intra-axonal volume fraction remained relatively stable. The fiber dispersion index of NODDI exhibited the most pronounced sensitivity to aging. In addition, changes of the DTI indices in this aging cohort were correlated mostly with the fiber dispersion index rather than the intracellular volume fraction of NODDI or the q-space measurements. While men and women did not differ in the aging rate, men tend to have higher intra-axonal volume fraction than women. This study demonstrates that advanced dMRI using a HYDI acquisition and compartmental modeling of NODDI can elucidate microstructural alterations that are sensitive to age and sex. Finally, this study provides insight into the relationships between DTI diffusion metrics and advanced diffusion metrics of NODDI model and q-space imaging.

© 2015 The Authors. Published by Elsevier Inc. This is an open access article under the CC BY-NC-ND license (<http://creativecommons.org/licenses/by-nc-nd/4.0/>).

Introduction

The normal adult brain undergoes substantial morphologic changes as it ages. As shown in postmortem studies, the brain parenchyma shrinks as the ventricles enlarge (Blinkov et al., 1968). The age-related structural changes of the brain may be quantified by magnetic resonance imaging (MRI), a safe, non-invasive, and non-radiating imaging technique (Jernigan et al., 1991; Pfefferbaum et al., 1994; Mueller et al., 1998). Specifically, Voxel-Based Morphometry (VBM) of T1-weighted images (Ashburner and Friston, 2000) is used extensively to study structural changes in normally aging brains (Walhovd et al., 2005; Fjell and Walhovd, 2010; Westlye et al., 2010; Walhovd et al.,

2011). Significant atrophy in gray matter has been reported using T1-weighted images (Walhovd et al., 2005; Fjell and Walhovd, 2010; Walhovd et al., 2011). There has been less focus on white matter, although as neurons are lost, white matter integrity may be jeopardized due to both myelin degeneration and axonal loss (Feldman and Peters, 1998; Sandell and Peters, 2001; Marner et al., 2003; Sandell and Peters, 2003).

In the present study, instead of volumetric measurements, we assessed microstructural changes of white matter in the human brain associate with normal aging using water diffusion as a probe. Diffusion MRI (dMRI) probes microstructures of the human brain by measuring water diffusion properties at the cellular level *in vivo* and non-invasively. The microarchitecture of the brain tissues creates restricting environments that shape the diffusion probability function of water molecules. Therefore, the properties of the diffusion function measured by dMRI allow investigators to quantitatively assess tissue microstructures (Callaghan and Codd, 1998). Changes in microstructures are

* Corresponding author at: Department of Radiology and Imaging Sciences, Center for Neuroimaging, Indiana University School of Medicine, 355 West 16th Street, Suite 4100, Indianapolis, IN 46202, USA.

E-mail address: yucwu@iupui.edu (Y.-C. Wu).

often the precursors of volumetric changes; thus, microstructural imaging biomarkers are potentially more sensitive and altered earlier than the conventional technique of volumetric assessment using T1-weighted volume-based morphometry.

Most, but not all, dMRI studies of aging and age-related disorders, such as Alzheimer's disease have used diffusion tensor imaging (DTI). DTI metrics, fractional anisotropy (FA), mean diffusivity (MD), and axial and radial diffusivities (AD, RD), have been used to evaluate white matter alterations in many aging related studies (Sullivan et al., 2001; Pfefferbaum et al., 2005; Sullivan and Pfefferbaum, 2006; Westlye et al., 2010; Wu et al., 2011a, 2011b; Lamar et al., 2014). While DTI metrics are widely used as an indicator for white matter integrity, their specific microstructural mechanisms remain unclear. The DTI model has two fundamental limitations (Wu, 2006; Assaf and Pasternak, 2008; Jones, 2008; Tournier et al., 2011). First, the DTI diffusion indices from single diffusion-weighting b-value shell and simple three-dimensional Gaussian model are average measurements of water diffusion from multiple compartments (e.g., extracellular and intracellular spaces). These compartments are likely to have different diffusivities, shapes, and orientations. Second, DTI cannot sufficiently describe water diffusion in areas of crossing, kissing, and fanning fibers (Alexander et al., 2001; Alexander et al., 2002; Wu, 2006; Jones, 2008; Tournier et al., 2011). Underestimation of fiber numbers/directions affects DTI scalar metrics: FA values may decrease to values similar to those of gray matter. The AD and RD are no longer valid because the parallel cylindrical model of white matter fibers is violated in cases of crossing fibers (Alexander et al., 2001; Wheeler-Kingshott and Cercignani, 2009). Further, a recent study showed that the prevalence of crossing fibers in the brain white matter is ~90%, which may explain the lower than expected pathologic specificity of DTI metrics in complex white matter areas of the brain (Sullivan and Pfefferbaum, 2006; Jones and Cercignani, 2010; Tournier et al., 2011; Jeurissen et al., 2013; Jones et al., 2013).

In a more realistic consideration, within any given imaging voxel, white matter may comprise various diffusion compartments. Researchers have modeled diffusion compartment as: fast and slow diffusion components (Clark and Le Bihan, 2000); anisotropic hindered and restricted compartments (Jespersen et al., 2010; Fieremans et al., 2011; De Santis et al., 2013); fast isotropic free water and anisotropic tissue compartments (Pasternak et al., 2009); three compartments of fast isotropic diffusion, restricted isotropic diffusion, and restrict anisotropic diffusion (Chiang et al., 2014); or three compartments of fast isotropic diffusion (e.g., cerebrospinal fluid (CSF)), anisotropic hindered diffusion (e.g., extracellular water), and highly restricted anisotropic diffusion (e.g., intra-axonal compartments) (Zhang et al., 2012). More complex models with more than three compartments have been proposed, however they come at the cost of prolonged imaging time. Two examples of such models include: (1) composite hindered and restricted model of diffusion (CHARMED) with one anisotropic hindered diffusion compartment and multiple anisotropic restricted compartments for crossing fibers (Assaf and Basser, 2005), and (2) restriction spectrum imaging (RSI) with axons modeled by a spectrum of rigid sticks of various sizes (White et al., 2013). Neurite orientation dispersion and density imaging (NODDI) models the diffusion-weighted signal as a combination of three basic compartments of CSF, extracellular, and intracellular described above. The NODDI model produces diffusion metrics representing tissue characteristics, including the orientation dispersion index (ODI) describing the degree of fanning/crossing of fibers and the intracellular volume fraction (ICVF) describing the axonal density under the rigid stick assumption. In a recent study, the ICVF of NODDI was in high agreement with the neurite compartment density measured by histology in an ex vivo mouse brain (Sepehrband et al., 2015). Thus, NODDI indices are potentially less ambiguous than DTI in the interpretation of diffusion-weighted microstructural characterization with increased specificity in clinical studies of the human brain. The NODDI model has been applied in studies of white matter changes

in aging relative studies (Kunz et al., 2014; Billiet et al., 2015; Chang et al., 2015; Nazeri et al., 2015), and other neurologic disorders (Adluru et al., 2014; Billiet et al., 2014; Winston et al., 2014; Timmers et al., 2015).

An alternative approach to study microstructural changes in white matter is q-space imaging. The q-space approach uses a Fourier relationship between the diffusion-weighted q-space signals and the diffusion displacement distribution (propagator) space. This is analogous to the relationship between k-space and image space in MRI. The water diffusion function, the probability density function (PDF) (Callaghan, 1991) also called mean apparent propagator (MAP) (Ozarslan et al., 2013) or ensemble average propagator (EAP) (Descoteaux et al., 2011; Hosseini et al., 2013), may be estimated through a q-space imaging formula. The PDF and the q-space diffusion signal have a Fourier Transform relationship: $P(\vec{R}, \Delta) = FT^{-1}[E_\Delta(\vec{q})]$, where P is PDF; \vec{R} is the displacement vector; Δ is the diffusion time; E is the normalized q-space signal; and \vec{q} is the q-space wavevector determined by the diffusion gradient strength (\vec{G}) and the duration (δ), $\vec{q} = \gamma \vec{G} \delta$ (Callaghan, 1991). The zero displacement probability, P_0 , is the return to origin probability ($P_0 = P(\vec{R} = 0, \Delta)$), and presents the probability of those water molecules having no net diffusion within a diffusion time Δ . P_0 is often interpreted as a measure of restricted diffusion and cellularity (Assaf et al., 2000; Wu and Alexander, 2007; Ozarslan et al., 2013). In an animal study of dysmyelination, P_0 has been found highly sensitive to the myelination and brain maturation (Wu et al., 2011a, 2011b) consistent with other studies of P_0 in demyelination of the human brain (Assaf et al., 2005).

In this study, we investigated the age-related changes and sex differences of microstructure-specific diffusion metrics in the brain of young to middle-aged adults. To distinguish multiple diffusion compartments with different diffusivities, we used hybrid diffusion imaging (HYDI) with multiple b-values (i.e., multiple shells) and multiple diffusion weighting directions in each shell to capture the directionalities of the diffusion compartments (Wu and Alexander, 2007). HYDI data is versatile and can be analyzed using DTI, multi-compartmental modeling (e.g., NODDI model), and the q-space approach. Therefore, HYDI enables a comprehensive investigation of the relationship between DTI metrics, NODDI indices, and q-space imaging metrics.

Materials and methods

Participants

Forty-seven (24 women and 23 men) right-handed healthy volunteers between 18 and 55 years of age were recruited for this study. All participants gave informed consent approved by the guidelines of the institutional review board at University of Wisconsin-Madison. Exclusion criteria included significant medical, neurological or psychiatric illness as determined by the in-house Brain Health Checklist and the Holden Psychological Screening Inventory (HPSI) (Holden, 1996). T1-weighted images of all subjects were reviewed by a neuroradiologist for incidental findings.

Imaging protocol

HYDI was performed on a 3.0-T GE-SIGNA scanner with an 8-channel head coil and ASSET parallel imaging ($R = 2$). The HYDI encoding scheme contained 5 concentric diffusion-weighting shells (b -values = 0, 375, 1500, 3375, 6000, 9375 s/mm²) and 126 diffusion-weighting gradient directions (Wu and Alexander, 2007, Table 1). The diffusion-weighted pulse sequence was a single-shot, spin-echo, echo-planar imaging (SS-SE-EPI) with pulse oximeter gating. The MRI parameters used were as follows: TR = 10–15 heartbeats (effective TR ~ 12–15 s), TE = 122 ms, FOV = 256 mm, matrix = 128 × 128,

Table 1

White matter ROIs, their acronyms, and sizes in number of voxels. Voxels are defined in the standard MNI space with an isotropic resolution of 1 mm. The color of the acronyms matches the ROIs shown in Fig. 2.

Symbol	Name	Voxels	Symbol	Name	Voxels
ACR	Anterior corona radiata	1616	PCR	Posterior corona radiata	788
ALIC	Anterior limb of internal capsule	806	PCT	Pontine crossing tract	464
BCC	Body of corpus callosum	3138	PLIC	Posterior limb of internal capsule	852
CGC	Cingulum (cingulate gyrus)	448	PTR	Posterior thalamic radiation	1097
CGH	Cingulum (hippocampus)	257	RLIC	Retrolenticular part of IC	749
CP	Cerebral penduncle	611	SCC	Splenium of corpus callosum	2298
CST	Corticospinal tract	385	SCP	Superior cerebellar peduncle	242
EC	External capsule	1381	SCR	Superior corona radiata	1287
Fx	Fornix (column and body of fornix)	146	SFO	Superior fronto-occipital fasciculus	82
Fx-ST	Fornix / Stria terminalis	357	SLF	Superior longitudinal fasciculus	1417
GCC	Genu of corpus callosum	1758	SS	Sagittal stratum	538
ICP	Inferior cerebellar penduncle	220	TAP	Tapatum	20
MCP	Middle cerebellar penduncle left	2578	UNC	Uncinate fasciculus	75
ML	Medial lemniscus	210			

voxel size = $2 \times 2 \text{ mm}^2$ interpolated (by zero filling in the k-space) to $1 \times 1 \text{ mm}^2$, 30 slices with slice thickness = 3 mm, and a total scan time of ~30 min. Diffusion parameters comprised a maximum b value of 9375 s/mm^2 , a diffusion gradient duration δ of 45 ms, and a diffusion gradient separation Δ of 56 ms. These corresponded to a q space sampling interval $\Delta q_r = 15.2 \text{ mm}^{-1}$, a maximum length of the q-space wavevector $q_{\max} = 76.0 \text{ mm}^{-1}$, a field of view of the diffusion displacement space $\text{FOV}_R = (1/\Delta q_r) = 65 \mu\text{m}$, and resolution of the diffusion displacement space $\Delta R = (1/2q_{\max}) = 6.6 \mu\text{m}$ (Callaghan, 1991). The FOV_R describes the width of the reconstructed displacement spectrum and the ΔR describes the resolution in the displacement space.

Image preprocessing

The diffusion-weighted images were corrected for motion and eddy current distortion artifacts using the *eddy_correct* (i.e., linear registration) tool from the diffusion processing toolbox in the FMRIB Software Library (FSL) (Jenkinson et al., 2002). Fieldmap correction was not performed. The HYDI data were used to compute diffusion metrics of DTI, NODDI and q-space imaging.

DTI metrics

DTI metrics were derived using the CAMINO diffusion image analysis software library (Cook et al., 2006) on the first (b -value = 375 s/mm^2) and second shells (b -value = 1500 s/mm^2) of the HYDI data (Wu and Alexander, 2007). DTI metrics were computed according to the formulas in (Basser et al., 1994):

$$AD = \lambda_1 \quad (1)$$

$$RD = (\lambda_2 + \lambda_3)/2 \quad (2)$$

$$MD = (\lambda_1 + \lambda_2 + \lambda_3)/3 \quad (3)$$

$$FA = \frac{\sqrt{3[(\lambda_1 - \langle \lambda \rangle)^2 + (\lambda_2 - \langle \lambda \rangle)^2 + (\lambda_3 - \langle \lambda \rangle)^2]}}{\sqrt{2(\lambda_1^2 + \lambda_2^2 + \lambda_3^2)}} \quad (4)$$

where $\langle \lambda \rangle = (\lambda_1 + \lambda_2 + \lambda_3)/3$.

λ_1 , λ_2 , and λ_3 are eigenvalues of the diffusion tensor. FA describes the coherence of the water diffusion; MD describes the mean water diffusion within an imaging voxel; AD describes the diffusion parallel to

the axonal direction; and RD describes the diffusion perpendicular to the axons.

NODDI metrics

All five HYDI shell data were used in the NODDI analysis using the toolbox (https://www.nitrc.org/projects/noddi_toolbox/). The NODDI model generates tissue-specific indices including ODI and ICVF by considering three basic diffusion compartments, as shown in Eq. (5):

$$A = (FISO)A_{iso} + (1 - FISO)((ICVF)A_{ic} + (1 - ICVF)A_{ec}), \quad (5)$$

where A is the measured diffusion signal, which is a summation of signals arising from three compartments: CSF (A_{iso}), intracellular spaces (A_{ic}), and extracellular space (A_{ec}). The data fitting in the NODDI model imposes hierarchical computation to separate the CSF and parenchyma first and subsequently separate the intracellular and extracellular compartment within the parenchyma. FISO denotes the volume fraction of fast isotropic diffusion compartment; (1-FISO) denotes the parenchymal volume fraction; the ICVF denotes the volume fraction of intracellular compartment (i.e., intra-axonal in white matter) within the parenchyma; and the volume fraction of the extracellular compartment within the parenchyma is (1-ICVF). The intra-axonal compartment was mathematically modeled with Watson distribution using cylindrical geometry. The cylindrical model assumes each axon to be made of sticks with zero radii (i.e., zero radial diffusivity) with axial diffusivity of $1.7 \times 10^{-3} \text{ mm}^2 \text{ s}^{-1}$. Therefore, in NODDI, axons are conceptualized as rigid sticks with fixed radial and longitudinal diffusivities. Such rigid sticks represent the “normal” axons, and the volume fraction of the sticks describes the volume fraction of normal axons. Under the assumption of a stick model with a zero radius, the volume fraction of the sticks (ICVF) represents “axonal density”. In addition to ICVF, the stick-like axon model also yields ODI from the Watson distribution describing the coherence of the sticks.

q-Space imaging metrics

All five HYDI shell data were used for q-space imaging analyses (Wu and Alexander, 2007). Given the Fourier relationship of the q-space diffusion signals and the diffusion probability density function, P_0 is

estimated by the volume integration of the q-space signals (central ordinate theorem) (Wu et al., 2008):

$$P_0 = P(\vec{R}, \Delta) = \int_{-\infty}^{\infty} E_{\Delta}(\vec{q}) d\vec{q} \approx \int_{-\vec{q}_{\max}}^{\vec{q}_{\max}} E_{\Delta}(\vec{q}) dq. \quad (6)$$

where E is the normalized q-space (i.e., diffusion) signal; Δ is the diffusion time; and \vec{q} is the q-space wavevector determined by the diffusion gradient strength (\vec{G}) and the duration (δ), $\vec{q} = \gamma \vec{G} \delta$ (Callaghan, 1991).

ROIs

Forty-eight regions of interest (ROIs) in white matter, including bilateral regions of the same anatomy, were considered in this study (Fig. 1). ROIs were defined in the standard MNI space and all the maps of diffusion metrics were non-linearly transformed to the standard space for statistical analysis. The FA map of the individual subject was non-linearly registered to the standard space FA image (FMRIB58_FA_1mm) using FSL registration tools FLIRT and FNIRT (Jenkinson et al., 2002; Andersson et al., 2007). The same

transformation matrix was applied to the other diffusion metrics. To avoid partial voluming effects from gray matter and CSF, white matter ROIs were highly selective by intersecting the white matter atlas, Johns Hopkins University (JHU) ICBM-DTI-81 (Oishi et al., 2008) with the common white matter skeleton created from all of the subjects (Fig. 1). The JHU white matter atlas is provided in FSL and the white matter skeleton was created using commands provided by the FSL in its Tract-Based Spatial Statistics (TBSS) toolbox (Smith et al., 2006). The definitions of the ROIs and voxel numbers are shown in Table 1.

Data analyses

The mean diffusion metrics in the ROIs for each subject were obtained to investigate age- and sex-related changes. The diffusion metrics were linearly regressed against age and sex using three regression models:

$$\text{Model 1 : } \text{diffusion-metric}_{\text{ROI}} = \beta_0 + \beta_1 \text{age} + \beta_2 \text{sex} + \beta_3 (\text{age} \times \text{sex}) + \text{error} \quad (7)$$

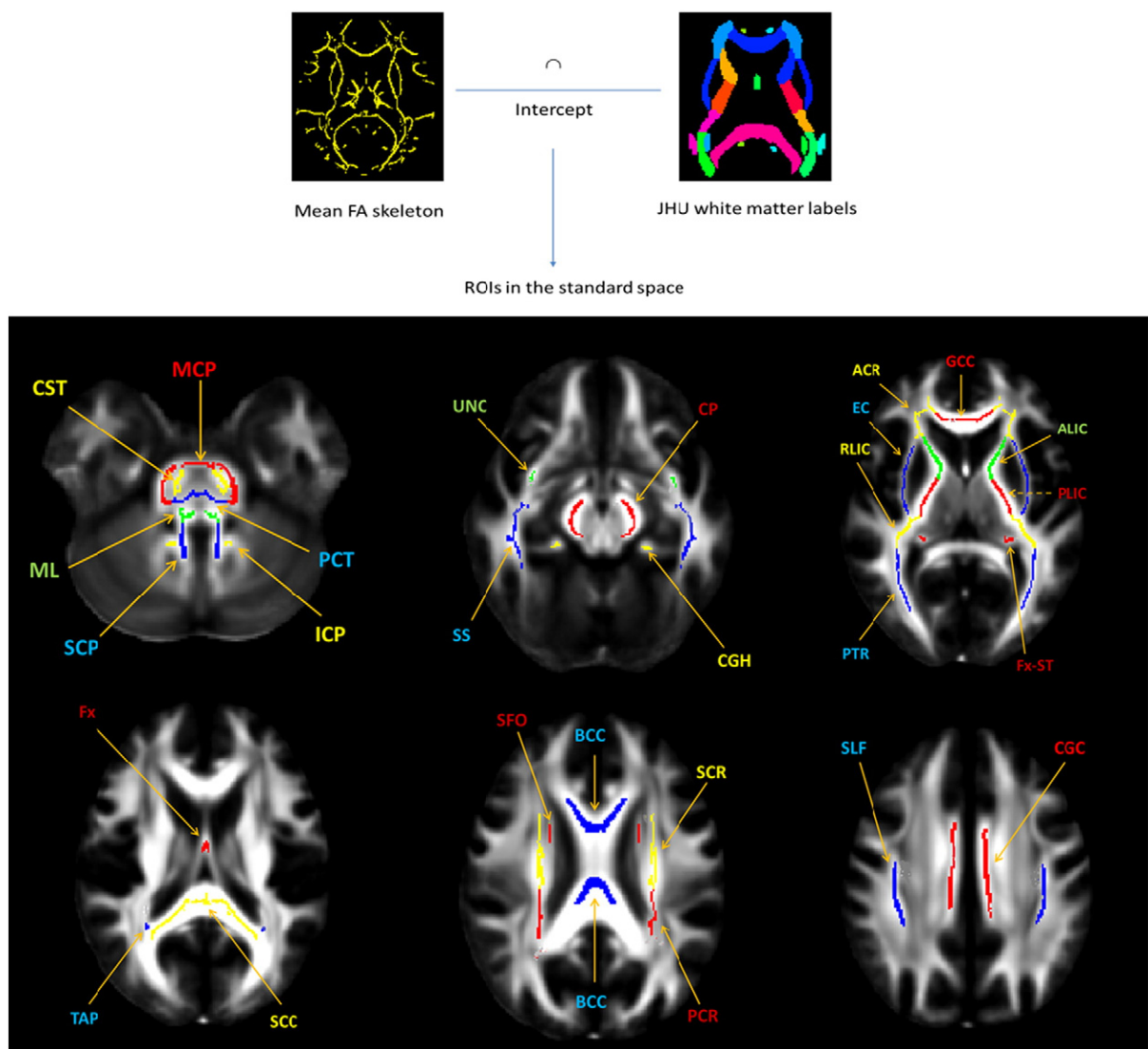


Fig. 1. Forty-eight white matter ROIs were defined in the standard MNI space by intersecting the mean FA skeleton and the white matter atlas. The mean FA skeleton was created by TBSS commands on the 47 subjects and the white matter atlas was provided by Johns Hopkins University (JHU) ICBM-DTI-81 in FSL. The bottom figure shows the 48 ROIs overlaid on the averaged FA map in the standard MNI space. The acronyms for the ROIs are listed in Table 1 with matching color.

$$\text{Model 2 : diffusion-metric}_{\text{ROI}} = \beta_0 + \beta_1 \text{age} + \beta_2 \text{sex} + \text{error} \quad (8)$$

$$\text{Model 3 : diffusion-metric}_{\text{ROI}} = \beta_0 + \beta_1 \text{age} + \text{error} \quad (9)$$

The β_0 , β_1 , β_2 , and β_3 are regression parameters. In the regression model 1 (Eq. 7), we test for significant age and sex interactions. In the regression model 2 (Eq. 8), we test for significant sex differences in the intercept assuming that the slopes are common for both sexes. In the regression model 3 (Eq. 9), we test for the age effects assuming that females and males have common age slope and common intercepts.

Selection of the regression model

Instead of imposing one model for all ROIs and all diffusion metrics, herein, we tested three possible linear models starting with Model 1, to address the diversity among ROIs and diffusion metrics. We ran a model selection procedure that follows the common practice of keeping regression factors when they are significant and removing non-significant regression factors to avoid overfitting (Draper and Smith, 1998). The basic rule follows a hierarchical workflow: if β_3 of model 1 is significant, model 1 is used; if β_2 of model 2 is significant, model 2 is used; otherwise, model 3 is used.

Model 1 with a higher level of complexity was first used to examine for sex differences in the rate of change in the diffusion measurements vs. age. If β_3 of model 1 is significant, it indicates that males and females have a different slope. Thus, model 1 is used for that diffusion metric in that particular ROI. Note that when β_3 is significant, β_2 may be either significant or not significant. A significant β_3 and β_2 indicates that the diffusion metric in that particular ROI has simultaneous sex differences in the rate of aging as well as a vertical shift difference. A significant β_3 , but not β_2 , indicates only sex differences in the aging rate. If β_3 of model 1 is not significant, model 1 can be degenerated to model 2. Model 2 was used to examine for “absolute” sex differences as in a vertical shift of the diffusion measurements. If β_2 of model 2 is significant, it indicates that females and males have different intercepts (i.e., a vertical shift). Thus, model 2 is used. If β_2 of model 2 is not significant, model 2 degenerates to model 3. Model 3 is the basic model assuming that females and males have the same rate of change and the same intercept. In summary, β_3 of model 1 describes the sex difference in the rate of aging, β_2 of model 1 and 2 describes the “absolute” sex difference, and β_1 of model 2 and 3 describes the common aging rate.

The goodness of the fit was evaluated using a residual analysis. An example of residual analysis is shown in supplementary Fig. S1 where (a) shows the residuals are randomly distributed around horizontal zero line, and (b) shows a linear quantile-quantile plot (Q-Q plot) indicating normal distribution of the residuals (Wilk and Gnanadesikan, 1968). Note that the diffusion metrics and age variable were not demeaned before fitting to the linear models. Correction for multiple comparisons was performed for the regression parameters (β_0 , β_1 , β_2 , and β_3) of each regression and across 48 ROIs using the false discovery rate (FDR) method. In addition, we also used a stricter multiple comparison correction utilizing the FDR method on 48 ROIs simultaneously on 7 diffusion metrics (i.e., 336 comparisons) to validate the high-prevalence significance of ODI. We report the results with the minimum FDR of less than 5% (i.e., q-value <0.05). Statistical analysis was performed using the R statistical software version R-3.2.2 (R Development Core Team, 2015).

TBSS analysis

Tract-based spatial statistics (TBSS) was performed on the diffusion metrics in the white matter skeleton of 47 subjects in the standard MNI space. To test the age effects and sex differences, the design and contrast matrix in Table S1 was used to test positive/negative correlations. The FSL *randomise* command with 5000 permutation was used to generate

the statistic maps. A threshold-free cluster enhancement with 2D optimization was used (Smith and Nichols, 2009). The corrected p-value maps adjusted for multiple comparisons across voxels in the white matter skeleton were produced for each row in the contrast matrix and for each diffusion metric.

Results

Among the 47 subjects (36 ± 11 (mean \pm SD) years old), women had a mean age of 38 ± 11 years old and men had a mean age of 34 ± 11 years old. The distribution of ages between women and men was not significantly different (ANOVA; all $p > 0.05$). All the residual plots and Q-Q plots were consistent with random normal distributions.

Maps of AD, RD, MD, FA, P_0 , ODI, and ICVF of one representative participant are shown in Fig. 2. AD and RD have high white matter contrast only in compact fiber tracts with known single fiber bundles, such as the corpus callosum, and the internal capsule. FA maps show high intensity in the white matter, indicating high tissue coherence, and low intensity in gray matter and CSF, indicating more isotropic diffusion (Fig. 2(d)). Consistently, white matter has a lower intensity in the ODI maps (Fig. 2(e)), indicating lower dispersion (i.e., high coherence). The P_0 map (Fig. 2(h)) shows higher intensity in more restricted areas (i.e., white matter), as expected. White matter also has a higher intensity than gray matter in the ICVF map (Fig. 2(f)), which represents higher intra-axonal volume fraction.

Sex differences

Sex differences in aging rate

Significant β_3 of the regression model 1 indicates that the rate of changes in the diffusion metrics was different in the brains of men and women. However, we did not find any ROI that had significant sex differences in aging rate.

Sex differences after adjusting for age

Significant β_2 of the regression model 2 (Eq. 8) indicates significant sex differences in intercepts, a vertical shift. Several ROIs had significant sex differences in the intercepts and most of the significances appeared in the diffusion metrics of the NODDI model: ODI and ICVF (Table 2). The regression lines of ICVF and ODI in age-critical ROIs were plotted in Fig. 3 to show the sex differences as in vertical shifts. The ODI of the male brains were ~7% significantly larger in the left fornix-stria terminalis and right superior corona radiata (~0.017 in absolute ODI value). ICVF was ~7% significantly higher in males in 13 ROIs including age-vulnerable anatomy (i.e., the right anterior segment of the cingulum, right hippocampal segment of cingulum, bilateral fornix-stria terminalis, and right uncinate fasciculus). A 7% of ICVF corresponds to 0.04 absolute differences. DTI and P_0 showed no significant sex differences in the intercepts of regression lines.

Aging effects

General trend and prevalence of age-sensitive diffusion metrics

Because all the diffusion metrics and ROI combinations had non-significant β_3 in regression model 1, the aging effects were the same for both sexes. Therefore, β_1 of either regression model 2 or regression model 3 was used to describe the common aging effect for both sexes. Table 3 summarizes those significant β_1 s (slope) across the white matter ROIs, and Fig. 4 shows the percentage changes of these slopes per decade. The significant regression lines for DTI and q-space analysis in age-critical ROIs are plotted in Fig. 5. Regression lines for ODI are plotted in Fig. 6. The general trend of age-related changes in diffusion metrics of DTI was decreased AD and increased RD followed by decreased FA. MD did not differ significantly over age. Similarly, tissue restriction (P_0) was relatively stable in most white matter ROIs, but decreased significantly in 2 ROIs including the uncinate fasciculus (UNC). The general

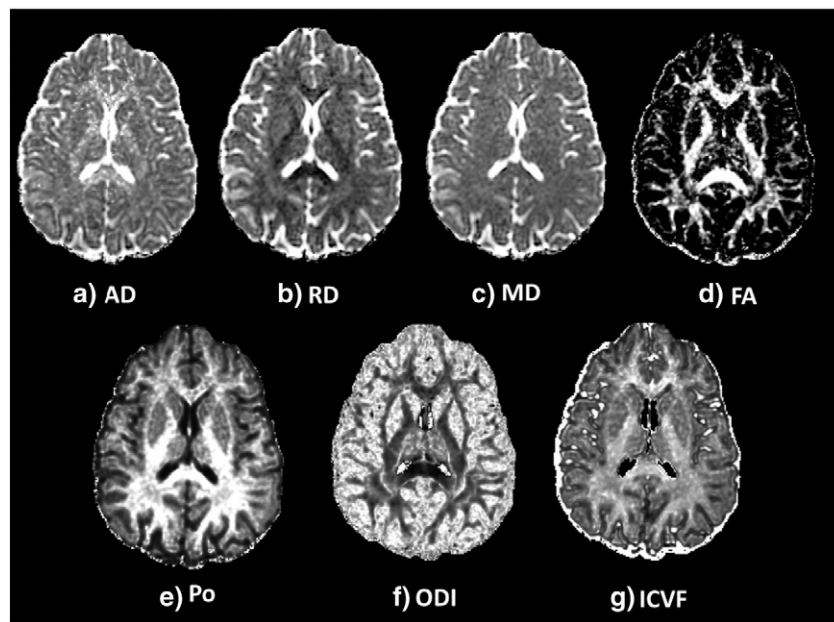


Fig. 2. Maps of the axial diffusivity (AD), radial diffusivity (RD), mean diffusivity (MD), and fractional anisotropy (FA) from DTI, and the tissue restriction index (P_0) from the q-space approach as well as the orientation dispersion index (ODI), and intracellular volume fraction (ICVF) from the NODDI model. The gray scales of AD, RD, and MD are 0 to 1.7, 1.1, $1.3 \times 10^{-3} \text{ mm}^2/\text{s}$, respectively. The FA map is scaled from 0.2 to 1. The P_0 , ODI, and ICVF maps are scaled from 0 to 1.

trend of age-related changes of NODDI metrics was increased fiber dispersion (ODI), which has the highest prevalence of significant white matter ROIs. The intra-axonal volume fraction (ICVF) was stable without significant changes in all white matter ROIs.

Relationships between the diffusion metrics

As shown in Table 3 and Table S2, 19% of FA-significant ROIs also had significantly decreased AD, and 76% of FA-significant ROIs had significantly increased RD. Together, there were 86% FA-significant ROIs with either decreased AD or increased RD. All FA-significant ROIs had increased ODI. All of AD- and RD-significant ROIs also had significantly ODI changes over age, except one RD-significant ROI. FA, AD, and RD did not correlate with ICVF or P_0 .

The quantitative age-related change in diffusion metrics

The percentage changes of the diffusion metrics across ROIs are shown in Fig. 4 (computed from β_1 in Table 3 and mean values in Table S3). AD decreased between 1% and 3% per decade. RD increased between 3% and 7.0% per decade in most ROIs, but surged to 12% in the right uncinate fasciculus. FA decreased between 1% and 8% per

decade. P_0 decreased 3% and 8%. ODI increased between 3% and 16%. Age-critical ROIs including the uncinate fasciculus, fornix and hippocampal segment of cingulum were often changed at higher rate than other white matter ROIs.

Age-sensitive white matter ROIs

Among the 48 white matter ROIs studied, the bilateral external capsule, retroレンtilular part of the internal capsule and uncinate fasciculus were the most sensitive to aging with 4 diffusion metrics having significant age-related changes (Table 3 and Fig. 4). The age-critical ROIs, including the left cingulum and fornix, had high sensitivity to aging with changes in 3 different diffusion metrics, whereas other age-critical ROIs, including the bilateral hippocampal segment of cingulum and fornix-stria terminalis, had moderate to low sensitivity. The bilateral anterior/superior/posterior corona radiata and sagittal stratum were moderately sensitive to aging. These white matter ROIs connect to cerebral cortices involving higher-level cognitive function. The white matter fibers connecting the left and right brain, the genu and splenium of the corpus callosum, were also sensitive to aging.

TBSS analysis

A subset of corrected p-values images for age effects in RD, FA, and ODI is shown in the top three rows of Fig. 7. While RD and ODI increased with age, FA decreased. AD, MD, P_0 and ICVF did not show age dependence in this young to middle-aged cohort using TBSS analysis. The bottom two rows of Fig. 7 show the spatial distribution of sex differences in ODI and ICVF. DTI and P_0 did not detect sex differences. In addition, males had higher ODI and ICVF than females. The full data can be downloaded at <http://dx.doi.org/10.7910/DVN/KUYSDI>.

Discussion

In this study, a flexible diffusion-weighted MRI method, HYDI, was used to investigate the relationships between diffusion metrics versus aging and sex in a healthy adult population. A strength of the HYDI method with five concentric diffusion-weighting shells is that it is versatile for multiple strategies of diffusion data processing

Table 2

Diffusion metrics and ROI pairs with a significant β_2 in model 2 (Eq. 8) indicating sex differences as a vertical shift, regardless of aging factors.

ROI	ODI (β_2)	ICVF (β_2)
ACR-L		0.039
ACR-R		0.031
ALIC-L		0.031
CGC-R		0.034
CGH-R		0.029
EC-R		0.024
Fx-ST-L	0.019	0.025
Fx-ST-R		0.034
PCT		0.032
PTR-R		0.034
SCR-R	0.014	
RLIC-L		0.025
RLIC-R		0.033
UNC-R		0.067

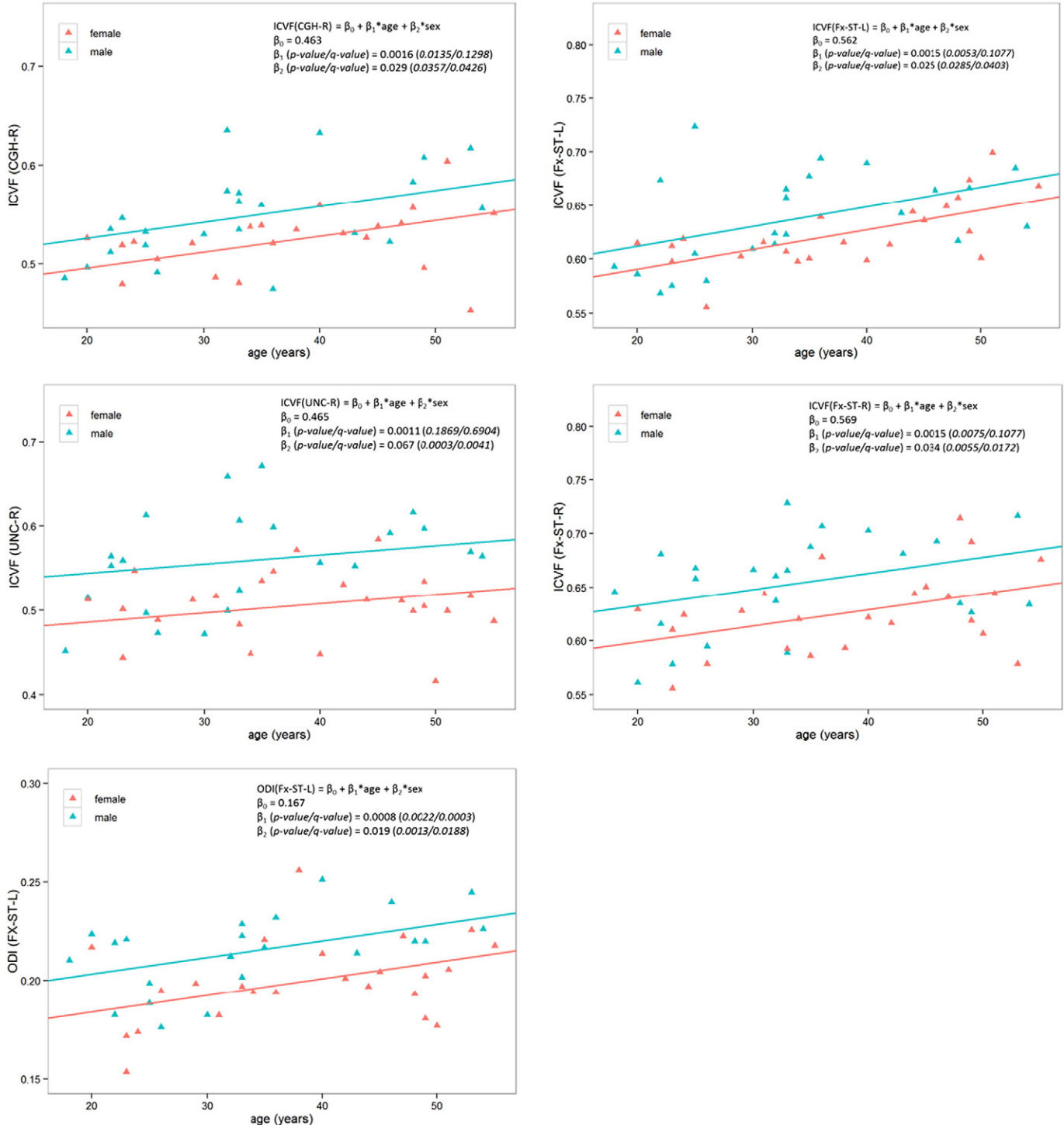


Fig. 3. Results of linear regression of model 2 for females (red) and males (blue). β_1 denotes the common aging rate for both females and males. β_2 denotes the amount of vertical shift (i.e., intercept) between females' and males' regression lines. P-value denotes the uncorrected significant level and the q-value denotes the false discovery rate (FDR) of the multiple comparisons across the 48 ROIs. Note that with the criteria of q-value < 0.05 for significance, most of β_2 s shown here are not significantly different from the null hypothesis, i.e., $\beta_2 = 0$, except ODI. However, the β_2 s shown here differ significantly between females and males.

(Wu and Alexander, 2007; Wu et al., 2008; Wu et al., 2011a, 2011b). The shell with a b-value of 1000 s/mm^2 is suitable for DTI, whereas the inner three shells with intermediate b-values may be further optimized for the NODDI model (Zhang et al., 2012), diffusion kurtosis model (DKI) (Fieremans et al., 2011), or diffusion basis spectrum imaging (DBSI) (Wang et al., 2011). The whole dataset is suitable for q-space analysis (Callaghan, 1991) or restriction spectrum imaging (RSI) (White et al., 2013). The outermost shell is a high angular

resolution diffusion imaging (HARDI) acquisition scheme (Frank, 2002; Tuch et al., 2002; Hess et al., 2006) and is suitable for q-ball imaging (QBI) to construct the fiber orientation distribution function (ODF) (Tuch, 2004) and white matter tractography. HYDI requires at least 126 diffusion directions, which require approximate 25 min of scan time with parallel imaging and less than 7 min with simultaneous multislice (SMS also called multi-band) technique (Setsompop et al., 2012).

Table 3

A summary of significant β_1 s, the common aging rate of the diffusion indices for both males and females. When β_2 of model 2 is significant, significant β_1 s of model 2 (Eq. 8) are listed (in bold italics). Significant β_1 s of model 3 (Eq. 9) are listed when β_2 of model 2 is not significant (meaning the regression model 2 degenerated to model 3). Full names of the white matter ROIs are listed in Table 1 and the anatomic locations are shown in Fig. 2.

ROI	AD (10^{-6} mm 2 /s year)	RD (10^{-6} mm 2 /s year)	FA/year (10^{-3})	Po/year (10^{-3})	ODI/year (10^{-3})
	β_1	β_1	β_1	β_1	β_1
ACR-L		1.098	−1.755		1.092
ACR-R		1.238	−1.634		1.113
ALIC-L	−1.997				1.240
ALIC-R	−1.724				1.162
BCC			−1.853		0.587
CGC-L		0.981	−1.382		1.022
CGC-R					1.110
CGH-L	−2.837				1.751
CGH-R					1.506
CP-L					0.829
CP-R					0.858
CST-L					0.668
CST-R					0.740
EC-L		2.580	−2.579		2.448
EC-R		2.481	−2.234	−1.662	1.967
Fx		6.843	−2.851		1.389
Fx-ST-L					0.842
Fx-ST-R		1.355			0.829
GCC		1.692	−1.888		0.772
ICP-L					0.780
ICP-R					0.596
MCP					
ML-L					0.904
ML-R					0.781
PCR-L		1.534	−1.372		0.724
PCR-R		1.279	−1.320		0.646
PCT					0.396
PLIC-L	−1.730				0.884
PLIC-R	−1.922				0.882
PTR-L		1.514	−1.975		1.231
PTR-R			−1.341		0.888
RLIC-L	−2.071	0.650	−1.412		1.035
RLIC-R			−1.054		0.964
SCC		1.061	−1.070		0.467
SCP-L					
SCP-R					
SCR-L	−1.009		−1.076		0.773
SCR-R	−1.297		−1.129		1.099
SFO-L					0.821
SFO-R					1.008
SLF-L					0.677
SLF-R					0.907
SS-L		0.841	−1.343		1.062
SS-R		0.815	−1.207		1.063
TAP-L					2.890
TAP-R					
UNC-L	−2.689	2.371	−3.766		3.345
UNC-R		4.587	−4.283	−3.002	3.497

Study considerations

The whole HYDI dataset was used for the NODDI computation in this study. Although the HYDI sampling scheme has more diffusion directions than the recommended NODDI sampling scheme (Zhang et al., 2012), approximately 2/3 of the diffusion signals are at higher b-value with lower signal-to-noise ratio (SNR). A computer simulation was performed to validate the compatibility of using the HYDI scheme for NODDI computation. Fig. 8 shows the simulation results at $\text{SNR}_{b0} = 20$, which is similar to the estimated white matter SNR of the human HYDI data in this study. The estimated SNR is approximately 21 ± 7 across the whole brain white matter of the 47 subjects at b-value = 0 s/mm 2 . Simulation results for other SNRs are in Fig. S2. Across the range of SNRs and ICVF-ODI combinations, the recommended NODDI

scheme and HYDI did not differ significantly from each other (p-value > 0.05). At $\text{SNR}_{b0} = 20$, HYDI overestimates low ICVFs more often than NODDI-p14, but both are comparable at a high ICVF (> 0.5), which is a more realistic value for white matter (Table S3). Both schemes underestimate high ODIs, but work fine at a low ODI (<= 0.5), which again is more realistic for white matter (Table S3).

The HYDI images were acquired at a voxel size of $2 \times 2 \times 3$ mm 3 . There may be partial voluming effects in the diffusion metrics due to the variation of size, angle, and curvature of white matter tracts across subjects (Vos et al., 2011). Thus, the group level analyses may be biased by these hidden covariates. To minimize the partial voluming effects, the white matter ROIs were limited at the center of the white matter bundle (i.e., white matter skeletons).

Age-related changes in DTI indices in white matter have been reported in literature, showing quadratic pattern changes with age. In particular, Westlye et al. reported extended results of quadratic changes of DTI indices in a group of 430 subjects ranging in age from 8 to 85 years old (Westlye et al., 2010). Nevertheless, liner models are appropriate for the young to middle-aged cohort in this study because: (1) in the paper by Westlye et al., the shapes of the quadratic curves for subjects between 18 and 55 years of age can be approximated by straight lines; and (2) both the residual and the Q-Q plots of the data in the present study showed no indications of non-linear relationships.

Aging effects

Age-sensitive white matter

Hippocampus-associated fiber tracts including the cingulum-hippocampal section and the limbic system (fornix, fornix-stria terminalis and uncinate fasciculus) were sensitive to aging. These findings support previous findings of aging related changes in gray matter using volumetric indices (Walhovd et al., 2011; Fjell et al., 2014) and NODDI metrics (Nazeri et al., 2015) as well as in white matter using voxel-based-morphometry (VBM) (Walhovd et al., 2005; Fjell and Walhovd, 2010), DTI (Westlye et al., 2010), and NODDI (Billiet et al., 2015). The aging effects on the hippocampal associated white matter fibers may explain the common amnesia syndrome in healthy older adults.

Microstructural changes in aging

In this young to middle-aged cohort, we found white matter fibers dispersed with aging in most white matter accompanied by relatively stable tissue restriction (P_0) and intra-axonal volume fraction (ICVF). P_0 is an index of tissue restriction and cellularity (Assaf et al., 2000; Wu and Alexander, 2007; Ozarslan et al., 2013), and also highly correlates with myelination in studies of an animal model of dysmyelination (Wu et al., 2011a, 2011b) and of the human brain with demyelination (Wu et al., 2011a, 2011b) and of the human brain with demyelination due to multiple sclerosis (Assaf et al., 2005). In this aging cohort, P_0 is relatively stable in most of the brain white matter, consistent with stable myelin-water fraction measured by multiple T2 relaxation in (Billiet et al., 2015). Nevertheless, P_0 did decrease significantly in aging-critical areas, the uncinate fasciculus, which may be explained by the pathologic findings of disrupted myelin in monkey studies (Sandell and Peters, 2001; Sandell and Peters, 2003) and substantial loss of myelinated fibers in the human brain (Marner et al., 2003). The age-related changes of ICVF have mixed results in previous studies. Increases of ICVF with age in white matter were found using a linear regression model in (Billiet et al., 2015) and using a logarithmic growth model in (Chang et al., 2015). Mixed increases and decreases of ICVF with age were found using a quadratic model in (Billiet et al., 2015). Interestingly, we did not find significant age-related changes in ICVF in all white matter ROIs, which may indicate the “axonal density” (Sepahband et al., 2015) is relatively stable in this middle-aged cohort. However, more evidence of direct measurements in animal models of aging or rapid post mortem imaging and histology studies may be needed to further validate and understand the role of ICVF index in aging.

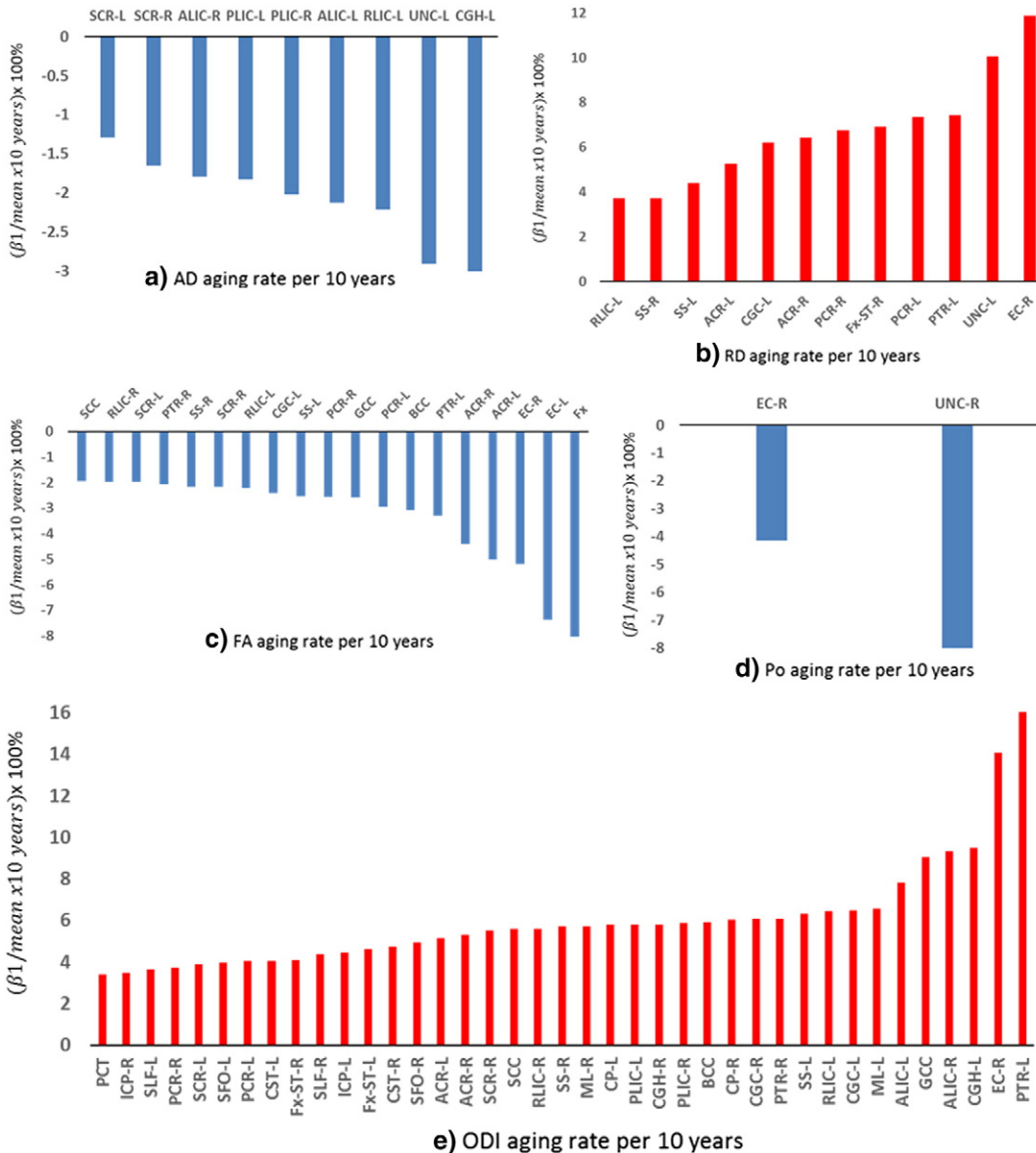


Fig. 4. Bar graphs of percentage changes in the diffusion metrics per decade across significant ROIs. Percent change per decade was computed using β_1 in Table 3 divided by the mean value of diffusion metrics across all subjects in Table S3, and multiplied by 10 years.

DTI vs. NODDI

Similar to all diffusion modeling, NODDI model has its own limitations such as the axons modeled as rigid sticks with a Watson distribution and a hierarchical fitting strategy (Zhang et al., 2012). In the NODDI framework, the rigid sticks describe axons with fixed intra-axonal diffusivities, whereas other diffusion models use “flexible” sticks and may yield estimates of intracellular diffusivities (Fieremans et al., 2011; Chiang et al., 2014). In addition, the Watson distribution is a unimodal distribution that assumes a single orientation for fiber bundles within an imaging voxel. Thus, similar to the major eigenvectors in DTI, NODDI yields a single directional vector as the estimate of overall fiber orientation within a voxel. Nevertheless, NODDI may provide some insights of specific microstructural metrics that may better characterize pathophysiologic changes than DTI indices. In contrast to the findings of Billiet et al. (Billiet et al., 2015), we found that ODI, instead of FA, was the diffusion metric most sensitive to aging with significant increases in 89% of the ROIs. This is probably due to slightly different

population and the use of a different approach to generate white matter ROIs. While both dispersion index and intracellular volume fraction could affect FA (Zhang et al., 2012), in our study, all of the changes in FA were accompanied with changes in ODI, but not ICVF because ICVF is not sensitive to this young to middle-aged cohort. Although FA is a dependent diffusion index derived from AD and RD, 14% of changes in FA could not be explained by either AD or RD, suggesting a lack of sensitivity. In addition, all of the AD- or RD-significant ROIs did not have alterations in tissue restriction or the freedom of diffusion (volume fractions), but were 100% correlated with the increase in fiber dispersion. Although AD and RD are sensitive to axonal integrity and myelination in animal studies (Song et al., 2002; Sun et al., 2005; Budde et al., 2009), in this aging cohort, changes in AD and RD merely reflected changes in the “organization” of fibers. Consistent with the previous suggestion in Wheeler-Kingshott and Cercignani (2009), this finding highlights the importance of cautions in interpreting DTI findings, especially AD and RD, on microstructural alterations in white matter.

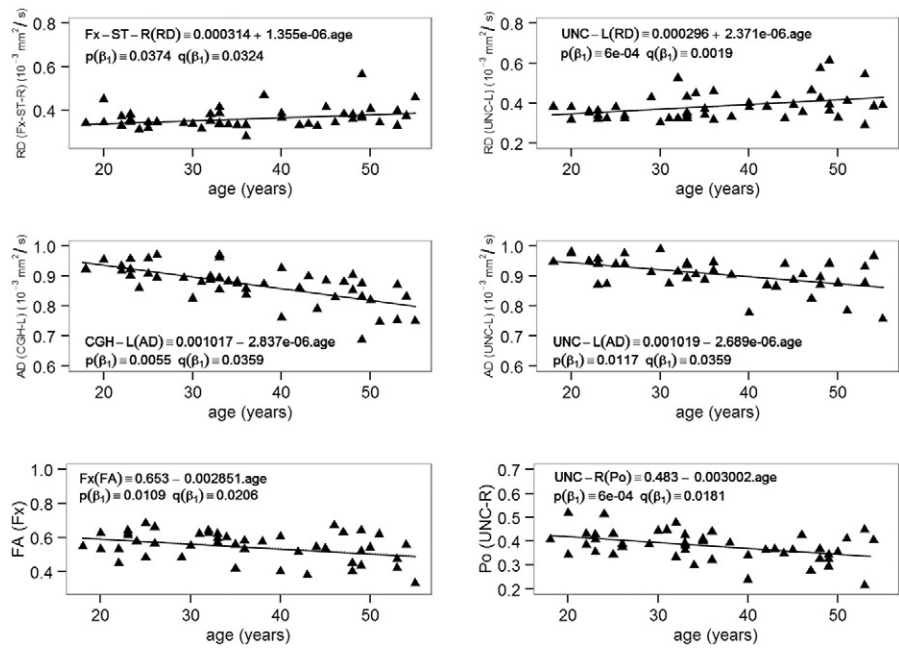


Fig. 5. Results of significant linear regression of model 3 for DTI (RD, AD, and FA) and q-space (P_0) metrics in age-critical ROIs including the fornix (Fx), fornix stria terminalis (Fx-ST), uncinate fasciculus (UNC), and cingulum hippocampal segment (CGH). The aging rate, β_1 , is also reported in Table 3. P-value denotes the uncorrected significant level and the q-value denotes the false discovery rate (FDR) of the multiple comparisons across the 48 ROIs. Q-value <0.05 is considered significant.

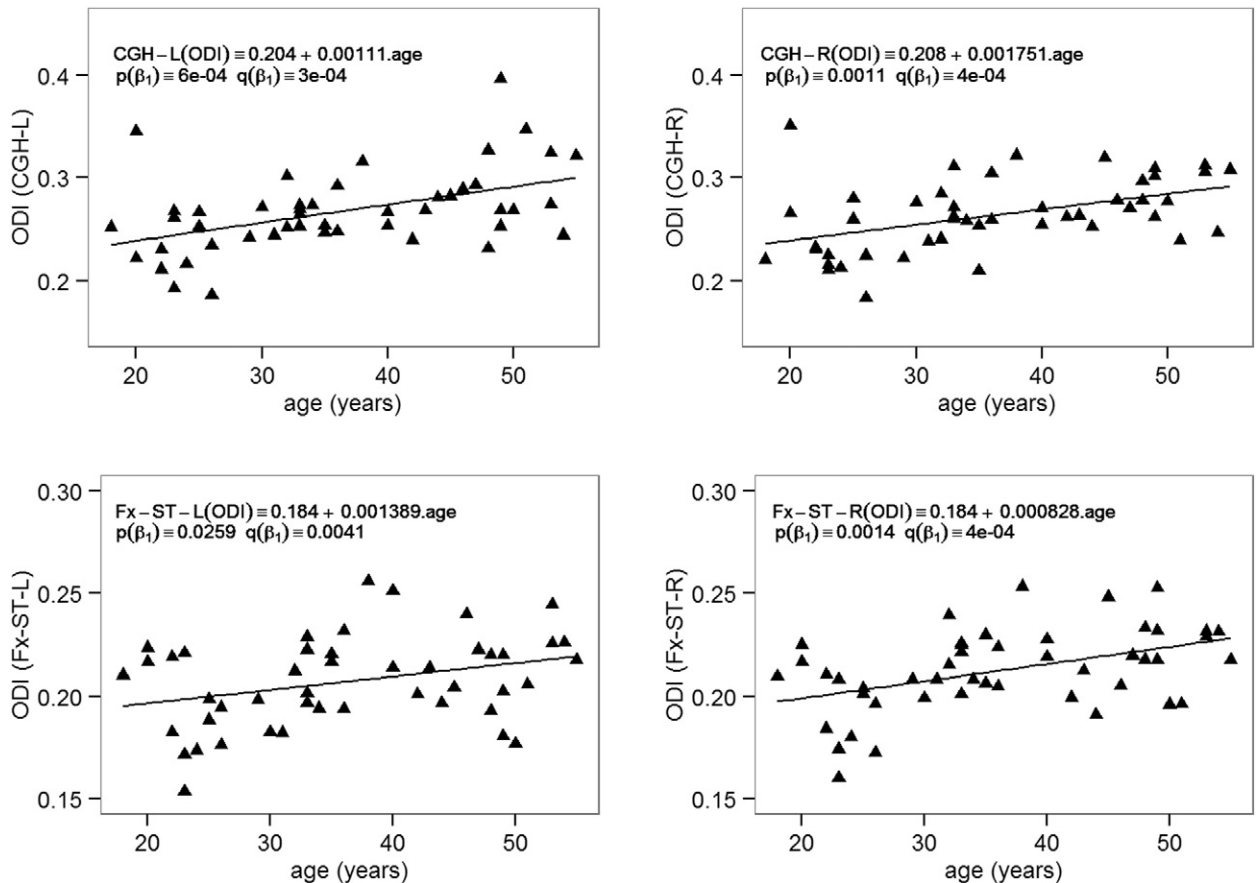


Fig. 6. Results of significant linear regression of model 3 for NODDI-ODI in age-critical ROIs including fornix stria terminalis (Fx-ST) and cingulum hippocampal segment (CGH). The aging rate, β_1 , is also reported in Table 3. P-value denotes the uncorrected significant level and the q-value denotes the false discovery rate (FDR) of the multiple comparisons across the 48 ROIs. Q-value <0.05 is considered significant.

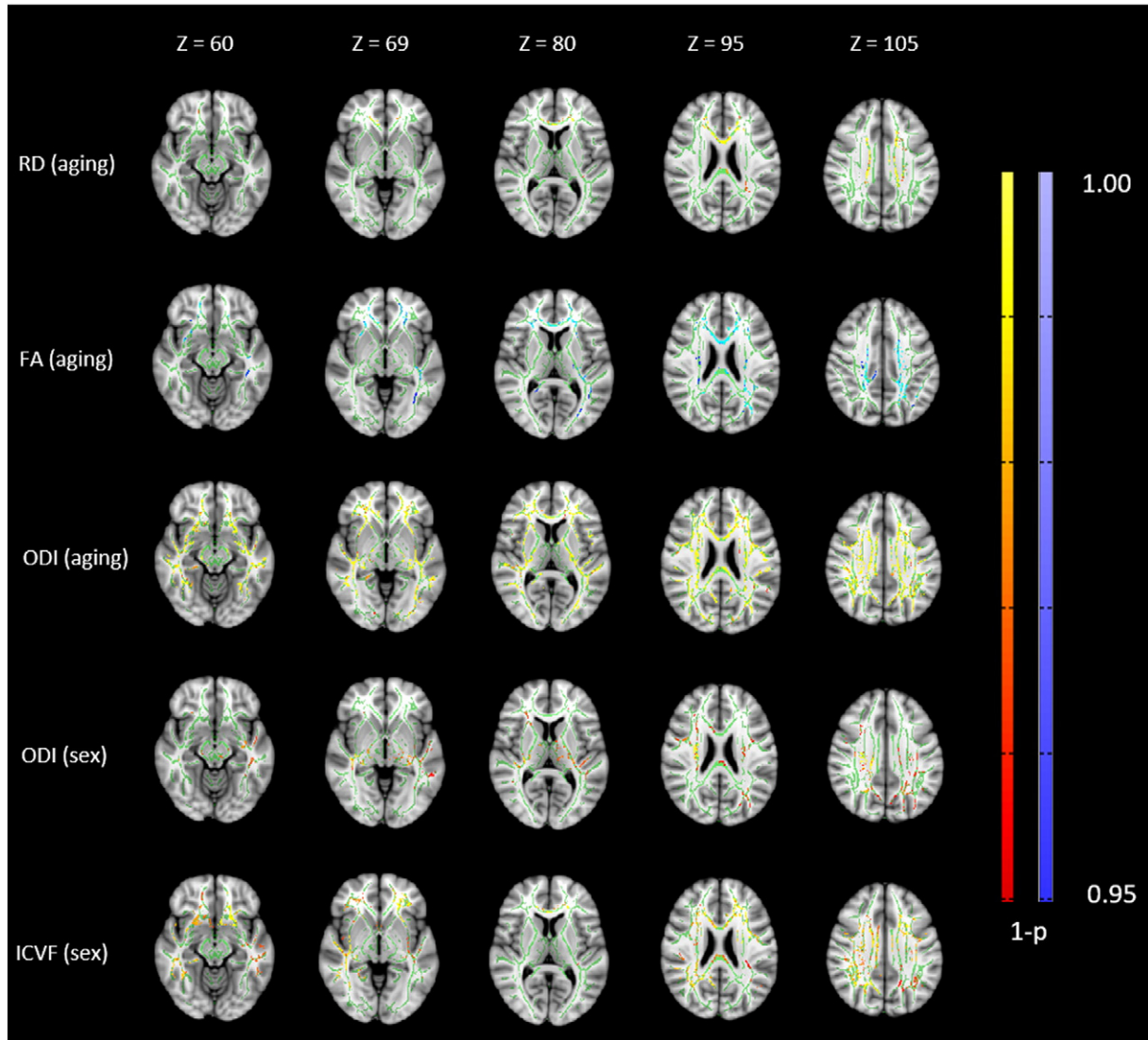


Fig. 7. TBSS analysis of diffusion metrics in the whole brain white matter skeleton to show the spatial distribution of age effects and sex differences. Maps of corrected p-value (as in $(1-p)$) overlaid on the standard T1W images. The green voxels indicate the white-matter skeleton. The red-yellow color code denotes positive correlation and blue-light blue color denotes negative correlation. The color scale is 0.95 to 1. The data is downloadable at <http://dx.doi.org/10.7910/DVN/KUYSDI>.

Sex differences

Reports using diffusion metrics from high-b-value experiments and compartmental modeling such as NODDI are limited in the literature. In this study, we found all of the white matter ROIs had no sex differences in the aging rate, but found that nearly 30% of the white matter ROIs had absolute sex differences. Interestingly, among the white matter ROIs that we found showed that significant sex differences also included the age-critical regions and the left fornix-stria terminalis was the most sensitive to sex difference. After adjusting for age, men tend to have higher intra-axonal volume fraction than women in 27% of the white matter ROIs and increase the fiber dispersion in 2 ROIs. Similar to the results in aging, NODDI indices are more sensitive than DTI in detecting sex differences.

TBSS and ROI

The results of the ROI analyses are consistent with the TBSS results in which ODI increased significantly over age in most of the white matter skeleton (Fig. 7) and MD, P_0 , and ICVF were not sensitive to aging. The TBSS analyses also showed similar trend of increased RD and ODI with

decreased FA over age. DTI and P_0 did not detect any sex difference using TBSS, which is also consistent to the ROI study. Similar to the ROI results in Table 2, the TBSS analyses show males had higher ODI and ICVF than females.

Conclusion

In this study, hippocampus-associated white matter tracts and white matter projecting to cerebral cortices were found to be sensitive to aging in young to middle-aged adults. Overall, aging led to greater dispersion of white matter fibers while the tissue restriction and intra-axonal volume fraction were relatively stable in most of the ROIs studied, except the uncinate fasciculus, which significantly decreased tissue restriction. The overall aging effects in the diffusion metrics were less than 10% per decade. The fiber dispersion index, ODI, of NODDI was more sensitive to aging than FA of DTI. In addition, most of the changes in AD and RD reflected changes in the fiber organization rather than in the freedom of diffusion. Despite that men and women did not differ in the aging rate, significant sex-difference with vertical shifts in the diffusion metrics were found in 30% of the white matter, in which men tend to have higher intra-axonal volume fraction. Similar

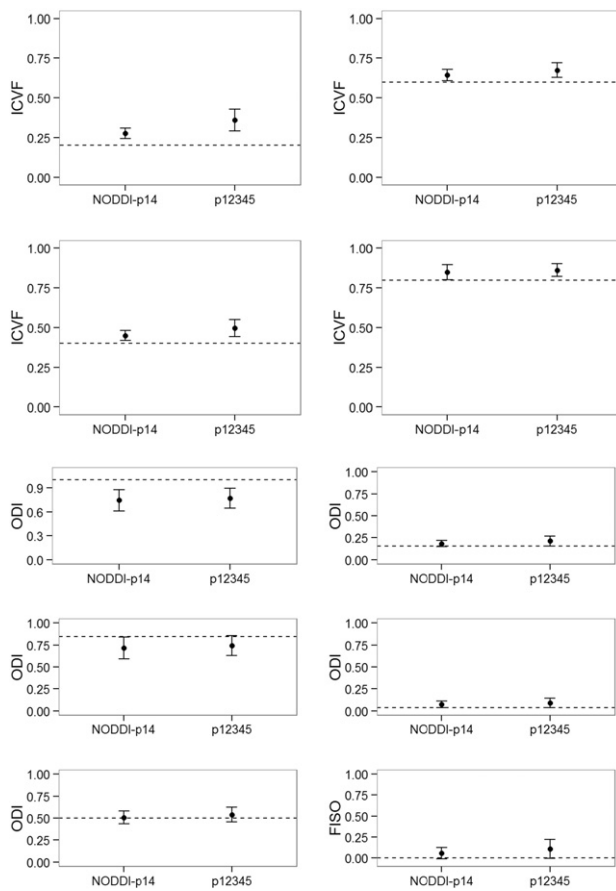


Fig. 8. Computer simulation of NODDI and HYDI schemes for NODDI computation. NODDI-p14 is the diffusion-encoding scheme recommended in the paper by Zhang et al. (2012). The p12345 is the HYDI 5-shell scheme used in this study. The dashed lines are ground truth: ICVF = [0.2, 0.4, 0.5, 0.8]; kappa = [0, 0.25, 1, 4, 16]; and FISO = 0. Kappa is the concentration parameter in the Watson distribution and relates to ODI by the following equation, ODI = $(2/\pi)\arctan(1/\kappa)$. There were 30 random trials at each of the 250 different fiber orientations that were uniformly distributed on a unit sphere. The SNR simulated was 20 at b -value = 0 s/mm², which is similar to the estimated white matter SNR of the HYDI human data in this study. For all the ICVF, the ODI simulated, NODDI-p14, and HYDI p12345 schemes did not significantly differ from each other (p -value > 0.05).

to the aging effects, the NODDI indices were more sensitive to sex differences than DTI.

Grant support

NIH R21 NS075791, NIH R01 MH062015, NIH P30 HD003352.

Appendix A. Supplementary data

Supplementary data to this article can be found online at <http://dx.doi.org/10.1016/j.neuroimage.2015.12.033>.

References

- Adluru, G., Gur, Y., Anderson, J.S., Richards, L.G., Adluru, N., DiBella, E.V., 2014. Assessment of white matter microstructure in stroke patients using NODDI. *Conf. Proc. IEEE Eng. Med. Biol. Soc.* 2014, 742–745.
- Alexander, A.L., Hasan, K.M., Lazar, M., Tsuruda, J.S., Parker, D.L., 2001. Analysis of partial volume effects in diffusion-tensor MRI. *Magn. Reson. Med.* 45 (5), 770–780.
- Alexander, D.C., Barker, G.J., Arridge, S.R., 2002. Detection and modeling of non-Gaussian apparent diffusion coefficient profiles in human brain data. *Magn. Reson. Med.* 48 (2), 331–340.
- Anderson, J.L., Jenkinson, M., Smith, S., 2007. Non-Linear Registration aka Spatial Normalisation. *FMRIB Technical Report TR07JA2*.
- Ashburner, J., Friston, K.J., 2000. Voxel-based morphometry—the methods. *NeuroImage* 11 (6 Pt 1), 805–821.
- Assaf, Y., Bassier, P.J., 2005. Composite hindered and restricted model of diffusion (CHARMED) MR imaging of the human brain. *NeuroImage* 27 (1), 48–58.
- Assaf, Y., Pasternak, O., 2008. Diffusion tensor imaging (DTI)-based white matter mapping in brain research: a review. *J. Mol. Neurosci.* 34 (1), 51–61.
- Assaf, Y., Mayk, A., Cohen, Y., 2000. Displacement imaging of spinal cord using q-space diffusion-weighted MRI. *Magn. Reson. Med.* 44 (5), 713–722.
- Assaf, Y., Chapman, J., Ben-Bashat, D., Hendler, T., Segev, Y., Korczyn, A.D., Graif, M., Cohen, Y., 2005. White matter changes in multiple sclerosis: correlation of q-space diffusion MRI and 1H MRS. *Magn. Reson. Imaging* 23 (6), 703–710.
- Basser, P.J., Mattiello, J., LeBihan, D., 1994. MR diffusion tensor spectroscopy and imaging. *Biophys. J.* 66 (1), 259–267.
- Billiet, T., Madler, B., D'Arco, F., Peeters, R., Deprez, S., Plasschaert, E., Leemans, A., Zhang, H., den Bergh, B.V., Vandenbulcke, M., Legius, E., Sunaert, S., Emsell, L., 2014. Characterizing the microstructural basis of “unidentified bright objects” in neurofibromatosis type 1: a combined *in vivo* multicomponent T2 relaxation and multi-shell diffusion MRI analysis. *NeuroImage Clin.* 4, 649–658.
- Billiet, T., Vandenbulcke, M., Madler, B., Peeters, R., Dhollander, T., Zhang, H., Deprez, S., Van den Bergh, B.R., Sunaert, S., Emsell, L., 2015. Age-related microstructural differences quantified using myelin water imaging and advanced diffusion MRI. *Neurobiol. Aging*.
- Blinkov, S.M., Glezer, I.A.I., Haigh, B., 1968. *The Human Brain in Figures and Tables: A Quantitative Handbook*. Basic Books; Plenum, New York.
- Budde, M.D., Xie, M., Cross, A.H., Song, S.K., 2009. Axial diffusivity is the primary correlate of axonal injury in the experimental autoimmune encephalomyelitis spinal cord: a quantitative pixelwise analysis. *J. Neurosci.* 29 (9), 2805–2813.
- Callaghan, P.T., 1991. *Principles of Nuclear Magnetic Resonance Microscopy*. Clarendon Press, Oxford.
- Callaghan, P.T., Codd, S.L., 1998. Generalised calculation of NMR imaging edge effects arising from restricted diffusion in porous media. *Magn. Reson. Imaging* 16 (5–6), 471–478.
- Chang, Y.S., Owen, J.P., Pojman, N.J., Thieu, T., Bukshpun, P., Wakahiro, M.L., Berman, J.L., Roberts, T.P., Nagarajan, S.S., Sherr, E.H., Mukherjee, P., 2015. White matter changes of neurite density and fiber orientation dispersion during human brain maturation. *PLoS One* 10 (6), e0123656.
- Chiang, C.W., Wang, Y., Sun, P., Lin, T.H., Trinkaus, K., Cross, A.H., Song, S.K., 2014. Quantifying white matter tract diffusion parameters in the presence of increased extra-fiber cellularity and vasogenic edema. *NeuroImage* 101, 310–319.
- Clark, C.A., Le Bihan, D., 2000. Water diffusion compartmentation and anisotropy at high b values in the human brain. *Magn. Reson. Med.* 44 (6), 852–859.
- Cook, P.B.Y., Nedjati-Gilani, S., Seunarine, K.K., Hall, M.G., Parker, G.J., Alexander, D.C., 2006. Camino: Open-Source Diffusion-MRI Reconstruction and Processing. *ISMRM, Seattle, WA, USA*.
- De Santis, S., Drakesmith, M., Bells, S., Assaf, Y., Jones, D.K., 2014. Why diffusion tensor MRI does well only some of the time: variance and covariance of white matter tissue microstructure attributes in the living human brain. *NeuroImage* 89, 35–44.
- Descoteaux, M., Deriche, R., Le Bihan, D., Mangin, J.F., Poupon, C., 2011. Multiple q-shell diffusion propagator imaging. *Med. Image Anal.* 15 (4), 603–621.
- Development Core Team, R., 2015. R: A Language and Environment for Statistical Computing Vienna, Austria. R Foundation for Statistical Computing.
- Draper, N.R., Smith, H., 1998. *Applied Regression Analysis*. Wiley-Interscience, United States of America.
- Feldman, M.L., Peters, A., 1998. Ballooning of myelin sheaths in normally aged macaques. *J. Neurocytol.* 27 (8), 605–614.
- Fieremans, E., Jensen, J.H., Helpern, J.A., 2011. White matter characterization with diffusional kurtosis imaging. *NeuroImage* 58 (1), 177–188.
- Fjell, A.M., Walhovd, K.B., 2010. Structural brain changes in aging: courses, causes and cognitive consequences. *Rev. Neurosci.* 21 (3), 187–221.
- Fjell, A.M., McEvoy, L., Holland, D., Dale, A.M., Walhovd, K.B., 2014. What is normal in normal aging? Effects of aging, amyloid and Alzheimer's disease on the cerebral cortex and the hippocampus. *Prog. Neurobiol.*
- Frank, L.R., 2002. Characterization of anisotropy in high angular resolution diffusion-weighted MRI. *Magn. Reson. Med.* 47 (6), 1083–1099.
- Hess, C.P., Mukherjee, P., Han, E.T., Xu, D., Vigneron, D.B., 2006. Q-ball reconstruction of multimodal fiber orientations using the spherical harmonic basis. *Magn. Reson. Med.* 56 (1), 104–117.
- Holden, R.R., 1996. Holden Psychological Screening Inventory Manual. Multi-Health Systems, North Tonawanda, NY.
- Hosseini, A.P., Chung, M.K., Wu, Y.C., Alexander, A.L., 2013. Bessel Fourier orientation reconstruction (BFOR): an analytical diffusion propagator reconstruction for hybrid diffusion imaging and computation of q-space indices. *NeuroImage* 64, 650–670.
- Jenkinson, M., Bannister, P., Brady, M., Smith, S., 2002. Improved optimization for the robust and accurate linear registration and motion correction of brain images. *NeuroImage* 17 (2), 825–841.
- Jernigan, T.L., Trauner, D.A., Hesselink, J.R., Tallal, P.A., 1991. Maturation of human cerebrum observed *in vivo* during adolescence. *Brain* 114 (Pt 5), 2037–2049.
- Jespersen, S.N., Bjarkam, C.R., Nyengaard, J.R., Chakravarty, M.M., Hansen, B., Vosegaard, T., Ostergaard, L., Yablonskiy, D., Nielsen, N.C., Vestergaard-Poulsen, P., 2010. Neurite density from magnetic resonance diffusion measurements at ultrahigh field: comparison with light microscopy and electron microscopy. *NeuroImage* 49 (1), 205–216.
- Jeurissen, B., Leemans, A., Tournier, J.D., Jones, D.K., Sijbers, J., 2013. Investigating the prevalence of complex fiber configurations in white matter tissue with diffusion magnetic resonance imaging. *Hum. Brain Mapp.* 34 (11), 2747–2766.
- Jones, D.K., 2008. Studying connections in the living human brain with diffusion MRI. *Cortex* 44 (8), 936–952.

- Jones, D.K., Cercignani, M., 2010. Twenty-five pitfalls in the analysis of diffusion MRI data. *NMR Biomed.* 23 (7), 803–820.
- Jones, D.K., Knosche, T.R., Turner, R., 2013. White matter integrity, fiber count, and other fallacies: the do's and don'ts of diffusion MRI. *NeuroImage* 93, 239–254.
- Kunz, N., Zhang, H., Vasung, L., O'Brien, K.R., Assaf, Y., Lazeyras, F., Alexander, D.C., Huppi, P.S., 2014. Assessing white matter microstructure of the newborn with multi-shell diffusion MRI and biophysical compartment models. *NeuroImage* 96, 288–299.
- Lamar, M., Zhou, X.J., Charlton, R.A., Dean, D., Little, D., Deoni, S.C., 2014. In vivo quantification of white matter microstructure for use in aging: a focus on two emerging techniques. *Am. J. Geriatr. Psychiatry Off. J Am. Assoc. Geriatr. Psychiatry* 22 (2), 111–121.
- Marner, L., Nyengaard, J.R., Tang, Y., Pakkenberg, B., 2003. Marked loss of myelinated nerve fibers in the human brain with age. *J. Comp. Neurol.* 462 (2), 144–152.
- Mueller, E.A., Moore, M.M., Kerr, D.C., Sexton, G., Camicioli, R.M., Howieson, D.B., Quinn, J.F., Kaye, J.A., 1998. Brain volume preserved in healthy elderly through the eleventh decade. *Neurology* 51 (6), 1555–1562.
- Nazeri, A., Chakravarty, M.M., Rotenberg, D.J., Rajji, T.K., Rathi, Y., Michailovich, O.V., Voineskos, A.N., 2015. Functional consequences of neurite orientation dispersion and density in humans across the adult lifespan. *J. Neurosci.* 35 (4), 1753–1762.
- Oishi, K., Zilles, K., Amunts, K., Faria, A., Jiang, H., Li, X., Akhter, K., Hua, K., Woods, R., Toga, A.W., Pike, G.B., Rosa-Neto, P., Evans, A., Zhang, J., Huang, H., Miller, M.I., van Zijl, P.C., Mazziotta, J., Mori, S., 2008. Human brain white matter atlas: identification and assignment of common anatomical structures in superficial white matter. *NeuroImage* 43 (3), 447–457.
- Ozarslan, E., Koay, C.G., Shepherd, T.M., Komlosh, M.E., Irfanoglu, M.O., Pierpaoli, C., Basser, P.J., 2013. Mean apparent propagator (MAP) MRI: a novel diffusion imaging method for mapping tissue microstructure. *NeuroImage* 78, 16–32.
- Pasternak, O., Sochen, N., Gur, Y., Intrator, N., Assaf, Y., 2009. Free water elimination and mapping from diffusion MRI. *Magn. Reson. Med. Off. J. Soc. Magn. Reson. Med. Soc. Magn. Reson. Med.* 62 (3), 717–730.
- Pfefferbaum, A., Mathalon, D.H., Sullivan, E.V., Rawles, J.M., Zipursky, R.B., Lim, K.O., 1994. A quantitative magnetic resonance imaging study of changes in brain morphology from infancy to late adulthood. *Arch. Neurol.* 51 (9), 874–887.
- Pfefferbaum, A., Adalsteinsson, E., Sullivan, E.V., 2005. Frontal circuitry degradation marks healthy adult aging: evidence from diffusion tensor imaging. *NeuroImage* 26 (3), 891–899.
- Sandell, J.H., Peters, A., 2001. Effects of age on nerve fibers in the rhesus monkey optic nerve. *J. Comp. Neurol.* 429 (4), 541–553.
- Sandell, J.H., Peters, A., 2003. Disrupted myelin and axon loss in the anterior commissure of the aged rhesus monkey. *J. Comp. Neurol.* 466 (1), 14–30.
- Sepahband, F., Clark, K.A., Ullmann, J.F., Kurniawan, N.D., Leanage, G., Reutens, D.C., Yang, Z., 2015. Brain tissue compartment density estimated using diffusion-weighted MRI yields tissue parameters consistent with histology. *Hum. Brain Mapp.* 36 (9), 3687–3702.
- Settempop, K., Gagowski, B.A., Polimeni, J.R., Witzel, T., Wedeen, V.J., Wald, L.L., 2012. Blipped-controlled aliasing in parallel imaging for simultaneous multislice echo planar imaging with reduced g-factor penalty. *Magn. Reson. Med.* 67 (5), 1210–1224.
- Smith, S.M., Nichols, T.E., 2009. Threshold-free cluster enhancement: addressing problems of smoothing, threshold dependence and localisation in cluster inference. *NeuroImage* 44 (1), 83–98.
- Smith, S.M., Jenkinson, M., Johansen-Berg, H., Rueckert, D., Nichols, T.E., Mackay, C.E., Watkins, K.E., Ciccarelli, O., Cader, M.Z., Matthews, P.M., Behrens, T.E., 2006. Tract-based spatial statistics: voxelwise analysis of multi-subject diffusion data. *NeuroImage* 31 (4), 1487–1505.
- Song, S.K., Sun, S.W., Ramsbottom, M.J., Chang, C., Russell, J., Cross, A.H., 2002. Dysmyelination revealed through MRI as increased radial (but unchanged axial) diffusion of water. *NeuroImage* 17 (3), 1429–1436.
- Sullivan, E.V., Pfefferbaum, A., 2006. Diffusion tensor imaging and aging. *Neurosci. Biobehav. Rev.* 30 (6), 749–761.
- Sullivan, E.V., Adalsteinsson, E., Hedenus, M., Ju, C., Moseley, M., Lim, K.O., Pfefferbaum, A., 2001. Equivalent disruption of regional white matter microstructure in ageing healthy men and women. *NeuroReport* 12 (1), 99–104.
- Sun, S.W., Song, S.K., Harms, M.P., Lin, S.J., Holtzman, D.M., Merchant, K.M., Kotyk, J.J., 2005. Detection of age-dependent brain injury in a mouse model of brain amyloidosis associated with Alzheimer's disease using magnetic resonance diffusion tensor imaging. *Exp. Neurol.* 191 (1), 77–85.
- Timmers, I., Zhang, H., Bastiani, M., Jansma, B.M., Roebroeck, A., Rubio-Gozalbo, M.E., 2015. White matter microstructure pathology in classic galactosemia revealed by neurite orientation dispersion and density imaging. *J. Inherit. Metab. Dis.* 38 (2), 295–304.
- Tournier, J.D., Mori, S., Leemans, A., 2011. Diffusion tensor imaging and beyond. *Magn. Reson. Med.* 65 (6), 1532–1556.
- Tuch, D.S., 2004. Q-ball imaging. *Magn. Reson. Med.* 52 (6), 1358–1372.
- Tuch, D.S., Reese, T.G., Wiegell, M.R., Makris, N., Belliveau, J.W., Wedeen, V.J., 2002. High angular resolution diffusion imaging reveals intravoxel white matter fiber heterogeneity. *Magn. Reson. Med.* 48 (4), 577–582.
- Vos, S.B., Jones, D.K., Viergever, M.A., Leemans, A., 2011. Partial volume effect as a hidden covariate in DTI analyses. *NeuroImage* 55 (4), 1566–1576.
- Walhovd, K.B., Fjell, A.M., Reinvang, I., Lundervold, A., Dale, A.M., Eilertsen, D.E., Quinn, B.T., Salat, D., Makris, N., Fischl, B., 2005. Effects of age on volumes of cortex, white matter and subcortical structures. *Neurobiol. Aging* 26 (9), 1261–1270 discussion 1275–1268.
- Walhovd, K.B., Westlye, L.T., Amlie, I., Espeseth, T., Reinvang, I., Raz, N., Agartz, I., Salat, D.H., Greve, D.N., Fischl, B., Dale, A.M., Fjell, A.M., 2011. Consistent neuroanatomical age-related volume differences across multiple samples. *Neurobiol. Aging* 32 (5), 916–932.
- Wang, Y., Wang, Q., Haldar, J.P., Yeh, F.C., Xie, M., Sun, P., Tu, T.W., Trinkaus, K., Klein, R.S., Cross, A.H., Song, S.K., 2011. Quantification of increased cellularity during inflammatory demyelination. *Brain* 134 (Pt 12), 3590–3601.
- Westlye, L.T., Walhovd, K.B., Dale, A.M., Bjørnerud, A., Due-Tonnesen, P., Engvig, A., Grydeland, H., Tamnes, C.K., Ostby, Y., Fjell, A.M., 2010. Life-span changes of the human brain white matter: diffusion tensor imaging (DTI) and volumetry. *Cereb. Cortex* 20 (9), 2055–2068.
- Wheeler-Kingshott, C.A., Cercignani, M., 2009. About "axial" and "radial" diffusivities. *Magn. Reson. Med.* 61 (5), 1255–1260.
- White, N.S., Leergaard, T.B., D'Arceuil, H., Bjaalie, J.G., Dale, A.M., 2013. Probing tissue microstructure with restriction spectrum imaging: histological and theoretical validation. *Hum. Brain Mapp.* 34 (2), 327–346.
- Wilk, M.B., Gnanadesikan, R., 1968. Probability plotting methods for the analysis of data. *Biometrika* 55 (1), 1–17.
- Winston, G.P., Micallef, C., Symms, M.R., Alexander, D.C., Duncan, J.S., Zhang, H., 2014. Advanced diffusion imaging sequences could aid assessing patients with focal cortical dysplasia and epilepsy. *Epilepsy Res.* 108 (2), 336–339.
- Wu, Y.C., 2006. Diffusion MRI: Tensors and Beyond PhD. University of Wisconsin-Madison.
- Wu, Y.C., Alexander, A.L., 2007. Hybrid diffusion imaging. *NeuroImage* 36 (3), 617–629.
- Wu, Y.C., Field, A.S., Alexander, A.L., 2008. Computation of diffusion function measures in q-space using magnetic resonance hybrid diffusion imaging. *IEEE Trans. Med. Imaging* 27 (6), 858–865.
- Wu, Y.C., Field, A.S., Duncan, I.D., Samsonov, A.A., Kondo, Y., Tudorascu, D., Alexander, A.L., 2011a. High b-value and diffusion tensor imaging in a canine model of dysmyelination and brain maturation. *NeuroImage* 58 (3), 829–837.
- Wu, Y.C., Field, A.S., Whalen, P.J., Alexander, A.L., 2011b. Age- and gender-related changes in the normal human brain using hybrid diffusion imaging (HYDI). *NeuroImage* 54 (3), 1840–1853.
- Zhang, H., Schneider, T., Wheeler-Kingshott, C.A., Alexander, D.C., 2012. NODDI: practical in vivo neurite orientation dispersion and density imaging of the human brain. *NeuroImage* 61 (4), 1000–1016.